MECSOL 2022 - Proceedings of the 8th International Symposium on Solid Mechanics
M.L. Bittencourt, J. Labaki, L.C.M. Vieira Jr. and E. Mesquita (Editors), Campinas SP, Brazil, October 17th to 19th, 2022

Vibration Energy Harvesting Using a Two-Degree of Freedom Duffing-type Structure

Luã Guedes Costa[1], Luciana Loureiro da Silva Monteiro[2] and Marcelo A. Savi[1]

[1] Universidade Federal do Rio de Janeiro, COPPE, Department of Mechanical Engineering, Center for Nonlinear Mechanics - Mecanon, Rio de Janeiro, Brazil
[2] Centro Federal de Educação Tecnológica Celso Suckow da Fonseca, CEFET/RJ, Department of Mechanical Engineering, Maracanã, Rio de Janeiro, Brazil

Abstract. The recent developments in technology and the emergence of Industry 4.0 have been motivating the study of optimized systems and new solutions to improve the employment of networks that use components as self-powered sensors, actuators and small electronic devices. In this regard, the scavenging of wasted forms of energy dissipated in the ambient is a topic that has been receiving great attention during the last few decades, especially the vibration energy. Composite structures utilizing piezoelectric materials are often employed to convert available mechanical energy into electrical energy exploiting the direct piezoelectric effect. In this work, a nonlinear two-degree of freedom Duffing-type energy harvesting system is proposed to enhance the performance of conventional devices. A discrete model is developed and numerical simulations are presented addressing the advantages and disadvantages of the system. Results show large operation bandwidths and power outputs, specially in higher frequencies.
Keywords: Energy Harvesting, Piezoelectric Materials, Nonlinear Dynamics, Chaos, Multiple DoF Systems.

INTRODUCTION

Recent developments in modern society demand for new solutions to power standalone small electronic devices. In this matter, piezoelectric materials have been shown to be a suitable alternative to harness wasted environmental mechanical energy as it has the property to convert mechanical energy into electrical energy by means of the direct piezoelectric effect. The direct piezoelectric effect occurs when a material is deformed and a proportional electrical charge is produced (Curie, 1889). Piezoelectric energy harvesters (PEHs) are usually based on cantilever beams, being designed to take advantage of the high strain near the clamped base of the structure (Erturk and Inman, 2008). This kind of system works as a resonator and its performance is interesting under resonant conditions. Several nonlinear characteristics were introduced to counteract the disadvantages of conventional devices. Among these, it should be pointed out the multistable systems that increase the overall efficiency and bandwidth of operation (Costa et al. 2021). It is also worth mentioning a promising recent concept of a nonlinear quasi-zero-stiffness energy harvester, that has been studied theoretically (Margielewicz et al., 2022). Additionally, the insertion of additional degrees of freedom proved to be a suitable way to increase the operation bandwidth even further (Tang and Yang, 2012). In this regard, Wu et al. (2012) proposed to add a second degree of freedom in the system as an inner beam, which narrow the band gap between natural frequencies, increasing the performance in a continuous interval of frequencies. This structure was enhanced by the addition of magnetic nonlinearities in the inner beam, which increased even further the performance of the energy harvester (Wu et al., 2014).

Inspired by the concept of multi-degree of freedom energy harvesters, this work deals with a generic duffing-type two-nonlinear-degrees of freedom energy harvester structure. A discrete model is developed as a proof of concept and numerical simulations are carried out driven by nonlinear dynamics and performance perspectives. A comparison with a basic version is established addressing the advantages and disadvantages of the proposed system.

PHENOMENOLOGICAL MODEL

Consider a prototype two-degree of freedom structure showed in Figure 1 that can be modelled assuming lumped masses in which the subscript $i = 1,2$ represents the properties related to each one of the two masses m_i, being k_i and c_i the equivalent stiffness and dissipation coefficients of the system. Piezoelectric patches are attached in the structure and are represented by electromechanical coupling coefficients θ_i, and a circuit with a simple load resistor R_{li} is attached to it. The piezoelectric material has a internal capacitance C_{pi} and an internal resistance of R_{pi}. The equivalent electrical resistance of the system R_i is composed by these two resistances connected in parallel, which means that $R_i = R_{li}R_{pi}/(R_{li}+R_{pi})$. In

addition, attached to both masses there are nonlinear elements, in which the equivalent restitution forces are dependent of the displacement z_i, measured with respect to the base that is excited by z_b.

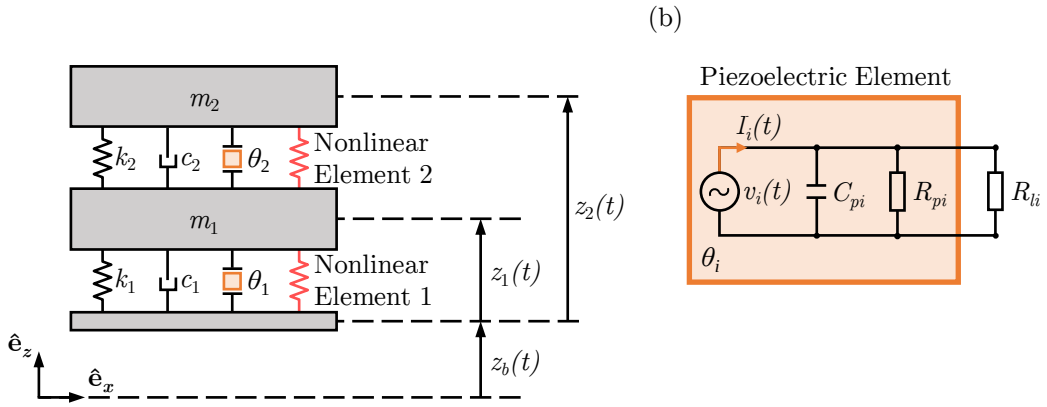

Figure 1 – (a) Lumped model representing a duffing-type two-degree of freedom energy harvesting structure. (b) Circuit representation of the piezoelectric element attached to a load resistance.

The nonlinear elements are described by a Duffing-type equation, represented by a cubic polynomial restitution forces, as follows:

$$f_1(z_1(t)) = -a_1 z_1(t) - b_1 z_1(t)^3 \tag{1}$$

$$f_2(z_2(t) - z_1(t)) = -a_2 \left[z_2(t) - z_1(t)\right] - b_2 \left[z_2(t) - z_1(t)\right]^3 \tag{2}$$

In which a_i and b_i, $i = 1,2$ are the polynomial restitution parameters. Under these assumptions, the kinetic and potential energies can be written as:

$$T = \frac{1}{2} m_1 \left[\dot{z}_1(t) + \dot{z}_b(t)\right]^2 + \frac{1}{2} m_2 \left[\dot{z}_2(t) + \dot{z}_b(t)\right]^2 \tag{3}$$

$$U = \frac{1}{2}(a_1 + k_1) z_1(t)^2 + \frac{1}{4} b_1 z_1(t)^4 + \frac{1}{2}(a_2 + k_2)\left[z_2(t) - z_1(t)\right]^2 + \frac{1}{4} b_2 \left[z_2(t) - z_1(t)\right]^4 \tag{4}$$

Piezoelectric effect is considered from the flux linkages $\dot{\lambda}_1(t) = v_1(t)$ and $\dot{\lambda}_2(t) = v_2(t)$, which allows the definition of the total piezoelectric coenergy (W_e) (Preumont, 2006):

$$W_e = \frac{1}{2} C_{p1} \dot{\lambda}_1(t)^2 + \theta_1 \dot{\lambda}_1(t) z_1(t) + \frac{1}{2} C_{p2} \dot{\lambda}_2(t)^2 + \theta_2 \dot{\lambda}_2(t) z_2(t) \tag{5}$$

The total energy dissipation can be described by Rayleigh's dissipation function (Meirovitch, 2010) and the electrical dissipation function as follows:

$$D = \frac{1}{2} c_1 \dot{z}_1(t)^2 + \frac{1}{2} c_2 \left[\dot{z}_2(t) - \dot{z}_1(t)\right]^2 + \frac{\dot{\lambda}_1(t)^2}{2R_1} + \frac{\dot{\lambda}_2(t)^2}{2R_2} \tag{6}$$

Therefore, the Lagrangian is defined by:

$$\mathcal{L} = T - U + W_e, \tag{7}$$

and with the Euler-Lagrange equation is associated with 2 mechanical variables and 2 electrical variables:

$$\frac{d}{dt}\left(\frac{\partial \mathcal{L}}{\partial \dot{q}}\right) - \frac{\partial \mathcal{L}}{\partial q} + \frac{\partial D}{\partial \dot{q}} = 0, \qquad q = [z_1(t), z_2(t), \lambda_1(t), \lambda_2(t)], \tag{8}$$

On this basis, since $\dot{q}(t) = dq(t)/dt$, the electromechanical equations of motion are given by

$$m_1\ddot{z}_1 + c_1\dot{z}_1 - c_2\left(\dot{z}_2 - \dot{z}_1\right) + \left(a_1 + k_1\right)z_1 + b_1 z_1^3 - \left(a_2 + k_2\right)\left(z_2 - z_1\right) - b_2\left(z_2 - z_1\right)^3 - \theta_1 v_1 = -m_1\ddot{z}_b \tag{9}$$

$$m_2\ddot{z}_2 + c_2\left(\dot{z}_2 - \dot{z}_1\right) + \left(a_2 + k_2\right)\left(z_2 - z_1\right) + b_2\left(z_2 - z_1\right)^3 - \theta_2 v_2 = -m_2\ddot{z}_b \tag{10}$$

$$C_{p1}\dot{v}_1 + \frac{v_1}{R_1} + \theta_1\dot{z}_1 = 0 \tag{11}$$

$$C_{p2}\dot{v}_2 + \frac{v_2}{R_2} + \theta_2\dot{z}_2 = 0 \tag{12}$$

A normalization of parameters is now in focus. Defining $\omega_i = \sqrt{k_i/m_i}$ $(i = 1,2)$ as references frequencies around one stable equilibrium point and considering a reference length, L, and a reference voltage, V, it is possible to write the dimensionless time, displacements and voltages as:

$$\tau = \omega_1 t, \qquad \bar{z}_i(\tau) = z_i(t)/L, \qquad \bar{v}_i(\tau) = v_i(t)/V, \qquad (i = 1,2) \tag{13}$$

The dimensionless energy harvesting governing equations can be written in a canonical form $\dot{\mathbf{q}} = \mathbf{f}(\mathbf{q})$, where the state variables are $\mathbf{q} = [\bar{z}_1, \dot{\bar{z}}_1, \bar{z}_2, \dot{\bar{z}}_2, \bar{v}_1, \bar{v}_2]$,

$$\begin{bmatrix} \dot{\bar{z}}_1 \\ \ddot{\bar{z}}_1 \\ \dot{\bar{z}}_2 \\ \ddot{\bar{z}}_2 \\ \dot{\bar{v}}_1 \\ \dot{\bar{v}}_2 \end{bmatrix} = \begin{bmatrix} \dot{\bar{z}}_1 \\ \gamma\Omega^2\sin(\Omega\tau) - 2\zeta_1\dot{\bar{z}}_1 + 2\zeta_2(\dot{\bar{z}}_2 - \dot{\bar{z}}_1) - \alpha_1\bar{z}_1 - \beta_1\bar{z}_1^3 + \alpha_2(\bar{z}_2 - \bar{z}_1) + \beta_2(\bar{z}_2 - \bar{z}_1)^3 + \chi_1\bar{v}_1 \\ \dot{\bar{z}}_2 \\ \gamma\Omega^2\sin(\Omega\tau) - \dfrac{2\zeta_2}{\rho}(\dot{\bar{z}}_2 - \dot{\bar{z}}_1) - \dfrac{\alpha_2}{\rho}(\bar{z}_2 - \bar{z}_1) - \dfrac{\beta_2}{\rho}(\bar{z}_2 - \bar{z}_1)^3 + \dfrac{\chi_2\bar{v}_2}{\rho} \\ -\varphi_1\bar{v}_1 - \kappa_1\dot{\bar{z}}_1 \\ -\varphi_2\bar{v}_2 - \kappa_2\dot{\bar{z}}_2 \end{bmatrix} \tag{14}$$

and the following dimensionless parameters arise:

$$\begin{aligned} &\zeta_1 = \frac{c_1}{2\omega_1 m_1}, \quad \zeta_2 = \frac{c_2}{2\omega_1 m_1}, \quad \bar{\alpha}_1 = \frac{a_1}{\omega_1^2 m_1}, \quad \bar{\alpha}_2 = \frac{a_2}{\omega_1^2 m_1}, \quad \beta_1 = \frac{b_1 L^2}{\omega_1^2 m_1}, \quad \beta_2 = \frac{b_2 L^2}{\omega_1^2 m_1} \\ &\gamma = \frac{A}{L}, \quad \Omega = \frac{\omega}{\omega_1}, \quad \rho = \frac{m_2}{m_1}, \quad \Omega_s = \frac{\omega_2}{\omega_1}, \quad \alpha_1 = 1 + \bar{\alpha}_1, \quad \alpha_2 = \Omega_s^2\rho + \bar{\alpha}_2, \quad \chi_1 = \frac{\theta_1 V}{\omega_1^2 m_1 L} \\ &\chi_2 = \frac{\theta_2 V}{\omega_1^2 m_1 L}, \quad \varphi_1 = \frac{1}{\omega_1 R_1 C_{p1}}, \quad \varphi_2 = \frac{1}{\omega_1 R_2 C_{p2}}, \quad \kappa_1 = \frac{\theta_1 L}{C_{p1} V}, \quad \kappa_2 = \frac{\theta_2 L}{C_{p2} V} \end{aligned} \tag{15}$$

Note that ζ_i is the mechanical dissipation, $\bar{\alpha}_i$ and β_i are nonlinear restitution parameters, ρ is the mass ratio, Ω_s is the ratio between natural frequencies, χ_i is the electromechanical coupling parameter in the mechanical equations, and κ_i is the new electromechanical coupling parameter in the electric equations. φ_i is the electric dissipation parameter. By considering a harmonic base excitation $\bar{z}_b = \gamma\sin(\Omega\tau)$, and its second derivative as $\ddot{\bar{z}}_b = -\gamma\Omega^2\sin(\Omega\tau)$, γ and Ω are the forcing amplitude and forcing frequency, respectively.

Performance Metrics

The performance of the energy harvesting system is evaluated with the definition of the converted electrical power by the piezoelectric element. Power is defined by the time rate of the work, thus the total electrical output power can be written as:

$$P_{\text{out}}^{(\text{total})} = P_{\text{out}_1}^{(\text{total})} + P_{\text{out}_2}^{(\text{total})} = \int_{t_0}^{t_f} \frac{v_1^2}{R_1}\,dt + \int_{t_0}^{t_f} \frac{v_2^2}{R_2}\,dt \tag{16}$$

Therefore, the instantaneous output power is given by:

$$P_{\text{out}} = \frac{v_1^2}{R_1} + \frac{v_2^2}{R_2} \tag{17}$$

The Root Mean Square (RMS) metric is interesting to be adopted as the main measurement, being defined as follows:

$$P_{\text{out}}^{\text{RMS}} = \frac{1}{t_f - t_0}\int_{t_0}^{t_f} P_{\text{out}}^2\,dt \tag{18}$$

The dimensionless counterparts of Equations 16, 17 and 18 are given by:

$$\bar{P}_{\text{out}}^{(\text{total})} = \bar{P}_{\text{out}_1}^{(\text{total})} + \bar{P}_{\text{out}_2}^{(\text{total})} = \int_{\tau_0}^{\tau_f} \left(\frac{\chi_1 \varphi_1}{\kappa_1} \bar{v}_1^2 + \frac{\chi_2 \varphi_2}{\kappa_2} \bar{v}_2^2 \right) d\tau \tag{19}$$

$$\bar{P}_{\text{out}} = \frac{\chi_1 \varphi_1}{\kappa_1} \bar{v}_1^2 + \frac{\chi_2 \varphi_2}{\kappa_2} \bar{v}_2^2 \tag{20}$$

$$\bar{P}_{\text{out}}^{\text{RMS}} = \frac{1}{\tau_f - \tau_0} \int_{\tau_0}^{\tau_f} \bar{P}_{\text{out}}^2 \, d\tau \tag{21}$$

STABILITY ANALYSIS

The equilibrium configurations of the system can be determined when both $d\mathbf{q}(\tau)/d\tau$ and $d\mathbf{q}^2(\tau)/d\tau^2$ are zero in a non-forced system ($\ddot{\bar{z}}_b = 0$). Therefore, solving $\dot{\mathbf{q}} = \mathbf{f}(\mathbf{q}) = 0$ yields up to 9 equilibrium points. By defining $\Gamma_1 = i\sqrt{\alpha_1/\beta_1}$ and $\Gamma_2 = i\sqrt{\alpha_2/\beta_2}$, in which $i = \sqrt{-1}$, it is possible to writte the equilibrium points as follows:

$$\text{EP}_1 = (\bar{z}_1, \dot{\bar{z}}_1, \bar{z}_2, \dot{\bar{z}}_2, \bar{v}_1, \bar{v}_2)_1 = (0,0,0,0,0,0) \tag{22}$$
$$\text{EP}_2 = (\bar{z}_1, \dot{\bar{z}}_1, \bar{z}_2, \dot{\bar{z}}_2, \bar{v}_1, \bar{v}_2)_2 = (0,0,\Gamma_2,0,0,0) \tag{23}$$
$$\text{EP}_3 = (\bar{z}_1, \dot{\bar{z}}_1, \bar{z}_2, \dot{\bar{z}}_2, \bar{v}_1, \bar{v}_2)_3 = (0,0,-\Gamma_2,0,0,0) \tag{24}$$
$$\text{EP}_4 = (\bar{z}_1, \dot{\bar{z}}_1, \bar{z}_2, \dot{\bar{z}}_2, \bar{v}_1, \bar{v}_2)_4 = (\Gamma_1,0,\Gamma_1,0,0,0) \tag{25}$$
$$\text{EP}_5 = (\bar{z}_1, \dot{\bar{z}}_1, \bar{z}_2, \dot{\bar{z}}_2, \bar{v}_1, \bar{v}_2)_5 = (-\Gamma_1,0,-\Gamma_1,0,0,0) \tag{26}$$
$$\text{EP}_6 = (\bar{z}_1, \dot{\bar{z}}_1, \bar{z}_2, \dot{\bar{z}}_2, \bar{v}_1, \bar{v}_2)_6 = (\Gamma_1,0,\Gamma_2+\Gamma_1,0,0,0) \tag{27}$$
$$\text{EP}_7 = (\bar{z}_1, \dot{\bar{z}}_1, \bar{z}_2, \dot{\bar{z}}_2, \bar{v}_1, \bar{v}_2)_7 = (\Gamma_1,0,-\Gamma_2+\Gamma_1,0,0,0) \tag{28}$$
$$\text{EP}_8 = (\bar{z}_1, \dot{\bar{z}}_1, \bar{z}_2, \dot{\bar{z}}_2, \bar{v}_1, \bar{v}_2)_8 = (-\Gamma_1,0,\Gamma_2-\Gamma_1,0,0,0) \tag{29}$$
$$\text{EP}_9 = (\bar{z}_1, \dot{\bar{z}}_1, \bar{z}_2, \dot{\bar{z}}_2, \bar{v}_1, \bar{v}_2)_9 = (-\Gamma_1,0,-\Gamma_2-\Gamma_1,0,0,0) \tag{30}$$

An analysis of these points shows that EP_1 always exists; EP_2 and EP_3 exist if $\text{sgn}(\alpha_2) \neq \text{sgn}(\beta_2)$; EP_4 and EP_5 exist if $\text{sgn}(\alpha_1) \neq \text{sgn}(\beta_1)$; EP_6, EP_7, EP_8 and EP_9 exist if $\text{sgn}(\alpha_1) \neq \text{sgn}(\beta_1)$ and $\text{sgn}(\alpha_2) \neq \text{sgn}(\beta_2)$.

The nature of stability of each equilibrium point can be determined evaluating the solution through a linearization of the system around each equilibrium point. By considering the Jacobian matrix $\mathbf{J}$ evaluated at each equilibrium point, and through its eigenvalues λ^{e}, the stability characteristics of these points are determined. On this basis, the eigenvalue spectrum of $\mathbf{J}$ can be classified in 3 sets: (1) Stable if $\{\lambda^{\text{e}} \in \mathbb{C} \mid \text{Re}(\lambda^{\text{e}}) < 0\}$, (2) Unstable if $\{\lambda^{\text{e}} \in \mathbb{C} \mid \text{Re}(\lambda^{\text{e}}) > 0\}$, and (3) Center if $\{\lambda^{\text{e}} \in \mathbb{C} \mid \text{Re}(\lambda^{\text{e}}) = 0\}$.

The stability of the linearized system at the vicinity of an equilibrium point corresponds to the stability of the associated nonlinear system, as long as that point is hyperbolic, which means that the Jacobian Matrix $\mathbf{J}$ has no eigenvalue that the real part vanishes ($\text{Re}(\lambda_k^{\text{e}}) \neq 0, \forall k$) (Savi, 2017). The Jacobian matrix of the the analyzed system is given by:

$$\mathbf{J} = \nabla^{\text{T}}\mathbf{f}(\bar{z}_1, \dot{\bar{z}}_1, \bar{z}_2, \dot{\bar{z}}_2, \bar{v}_1, \bar{v}_2) = $$
$$= \begin{bmatrix} 0 & 1 & 0 & 0 & 0 & 0 \\ -\alpha_1 - \alpha_2 - 3\left[\beta_1 \bar{z}_1^2 + \beta_2 (\bar{z}_2 - \bar{z}_1)^2\right] & -2(\zeta_1 + \zeta_2) & \alpha_2 + 3\beta_2 (\bar{z}_2 - \bar{z}_1)^2 & 2\zeta_2 & \chi_1 & 0 \\ 0 & 0 & 0 & 1 & 0 & 0 \\ \frac{1}{\rho}\left[\alpha_2 + 3\beta_2 (\bar{z}_2 - \bar{z}_1)^2\right] & \frac{2\zeta_2}{\rho} & -\frac{1}{\rho}\left[\alpha_2 + 3\beta_2 (\bar{z}_2 - \bar{z}_1)^2\right] & -\frac{2\zeta_2}{\rho} & 0 & \chi_2 \\ 0 & -\kappa_1 & 0 & 0 & -\varphi_1 & 0 \\ 0 & 0 & 0 & -\kappa_2 & 0 & -\varphi_2 \end{bmatrix} \tag{31}$$

The stability analysis can be complemented by the point of view of the potential energy function, determined in its dimensionless form by:

$$\bar{U} = \frac{1}{2}\alpha_1 \bar{z}_1^2 + \frac{1}{4}\beta_1 \bar{z}_1^4 + \frac{1}{2}\alpha_2 (\bar{z}_2 - \bar{z}_1)^2 + \frac{1}{4}\beta_2 (\bar{z}_2 - \bar{z}_1)^4 \tag{32}$$

Figure 2 shows some examples of possible equilibrium configurations of the system. Diamond shaped red dots represent unstable equilibrium points, while circular shaped blue dots represent stable equilibrium points, and they are associated with Equations 22 to 30. Energy levels associated with the potential energy function $\bar{U}$ are depicted by the color scale; darker colors represent potential wells (low energy levels), while lighter colors represent higher energy levels. Figure 2(a) represents a case in which both beams present monostability. Figure 2(b) shows a case in which $\bar{z}_1$ direction presents bistability and $\bar{z}_2$ direction presents monostability. In contrast, Figure 2(c) shows the opposite: monostability in $\bar{z}_1$ direction and bistability in $\bar{z}_2$ direction. Finally, Figure 2(c) represents a case in which both directions present bistability. Each of these equilibrium configurations can be achieved by tuning the nonlinear restitution force of the system.

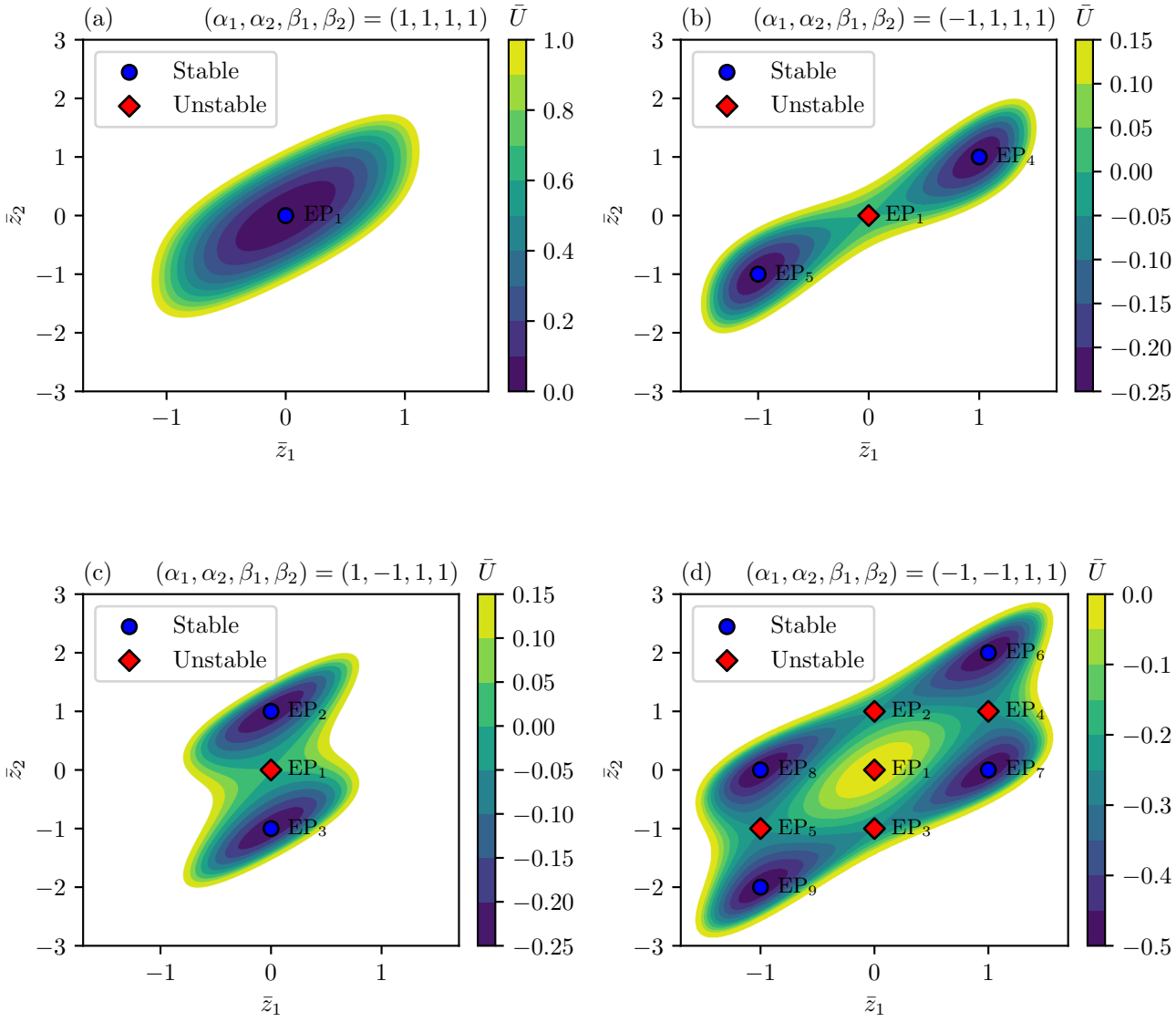

Figure 2 – Equilibrium points and potential energy levels for different equilibrium configurations.

NUMERICAL ANALYSIS

In this section, numerical simulations are performed employing the fourth order Runge-Kutta method in order to solve the nonlinear system of electromechanical equations $\dot{\mathbf{q}} = \mathbf{f}(\mathbf{q})$. A total of $n_p = 1000$ forcing periods are analyzed in each case. The equilibrium configuration D, depicted in Figure 2(d) is chosen to be analyzed. Dynamical response diagrams and Lyapunov exponent diagrams containing 501x501 different samples are built in order to map and identify different kinds of periodic and aperiodic attractors on the Ω and γ parameter domain. The procedure to classify different attractors

is based on the comparison of the magnitude of Lyapunov exponents and the verification of the steady state Poincaré map of the time series in each sample. Lyapunov exponent spectrum are examined utilizing the method of Wolf et al. (1985), and then compared, in two distinct initial time stages $\tau_0 = 0$ and $\tau = 0.75\tau_f$ (steady state), in order to ensure exponent convergence on samples that show long transient chaos orbits; $\tau_f = 2\pi n_p/\Omega$ is the final integration time. Results are classified based on the following attractors: Period-1 (dark gray), Period-2 (yellow), Period-3 (green), Period-4 (orange), Period-5 (purple), Period-6 or greater (light blue), Chaotic (red) and Hyperchaotic (dark red). Each point in the diagrams is the result of a numerical integration starting from a specific initial condition based on a stable equilibrium point of the analyzed configuration.

Table 1 – Fixed parameters employed on the numerical analyses.

ζ_1	ζ_2	ρ	Ω	γ	χ_1	χ_2	φ_1	φ_2	κ_1	κ_2
0.025	0.025	1	$0.01 \rightarrow 3$	$0.01 \rightarrow 1$	0.05	0.05	0.05	0.05	0.5	0.5

This section considers two different ideal cases in which both masses are equal in properties. The first case (Basic Configuration) is inspired on cases found in the literature that consider nonlinearities only in z_2 direction, while the second case is based on the equilibrium configuration D, that presents the most complex configuration in terms of equilibrium positions containing nonlinearities in both z_1 and z_2 directions. Table 1 summarizes the parameters employed in all analyses and Table 2 shows the parameters that distinguish each configuration analyzed.

Table 2 – Variable parameters and its respective cases.

Analyzed Case	α_1	α_2	β_1	β_2	Initial Condition
Basic Configuration	1	-1	0	1	EP_2
Equilibrium Configuration D	-1	-1	1	1	EP_6

Initially, consider the nonlinear dynamics characteristics of two configurations presented in Table 2: the basic configuration, which has two-degree of freedom, being one elastic; and configuration D, proposed in this work, which is a two-degree of freedom Duffing-type system. Figure 3 presents results of the basic configuration, while Figure 4 presents the results of the configuration D. Results are presented in the form of dynamical attractor diagrams and the two largest Lyapunov exponent diagrams, λ_1 and λ_2. Note that period-1, chaotic and hyperchaotic dynamics prevail in both cases. Also, for the configuration D, the appearance of robust zones of period-2 motion and a large non-robust zone of period-3 motion are observed, while robust period-4 and period-6+ zones are found for the basic configuration case. The difference between periodic and aperiodic dynamics is based on the rate of divergence of nearby orbits, being expressed by the Lyapunov exponents. The response is chaotic when the largest Lyapunov exponent λ_1 is positive (that is, the system presents a divergent direction in the phase space), quasiperiodic when the largest exponent is zero (that is, the direction is not divergent or convergent), and periodic when it is negative (convergent). Besides, a system is hyperchaotic when more than one directions are divergent in the phase space or, equivalently, when it has at least two positive exponents. This is illustrated in the Lyapunov exponent diagrams, in which rainbow colors represent positive exponents, while negative exponents are represented by the grayscale tones. On that matter, see that chaotic regions (red) present positive λ_1 and negative λ_2. On the other hand, hyperchaotic regions (dark red) present both λ_1 and λ_2 positive, and periodic attractors show negative λ_1 and λ_2.

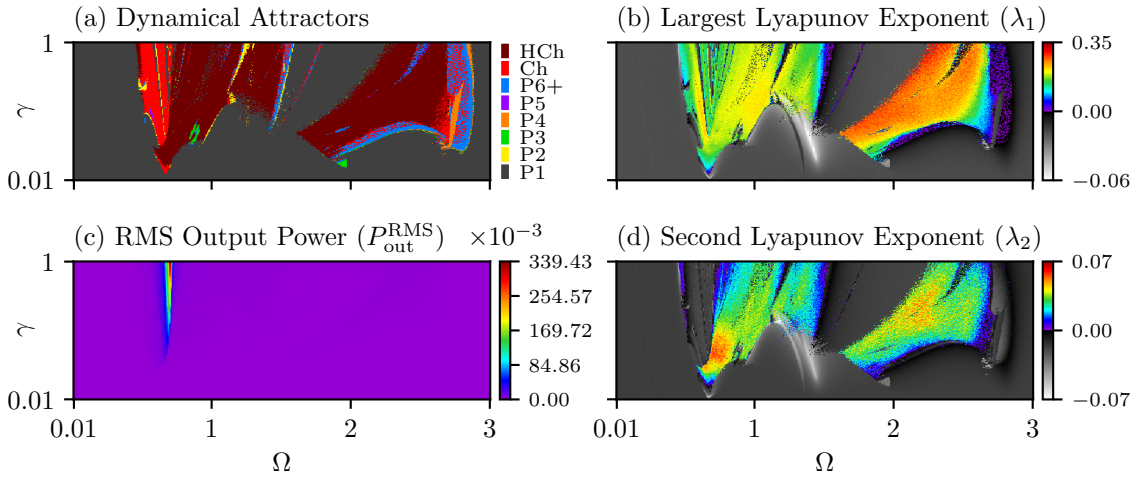

Figure 3 – Harvester proposed by Wu et al. (2014): (a) Attractors based on the dynamical response of the system. P# $(\#=1,2,3,4,5,6+)$ stands for periodic motion, while Ch and HCh shows chaotic and hyperchaotic motion, respectively; (b) Largest Lyapunov exponent (λ_1) diagram; RMS Output Power ($P_{\text{out}}^{\text{RMS}}$) diagram; (d) Second Lyapunov exponent (λ_2) diagram.

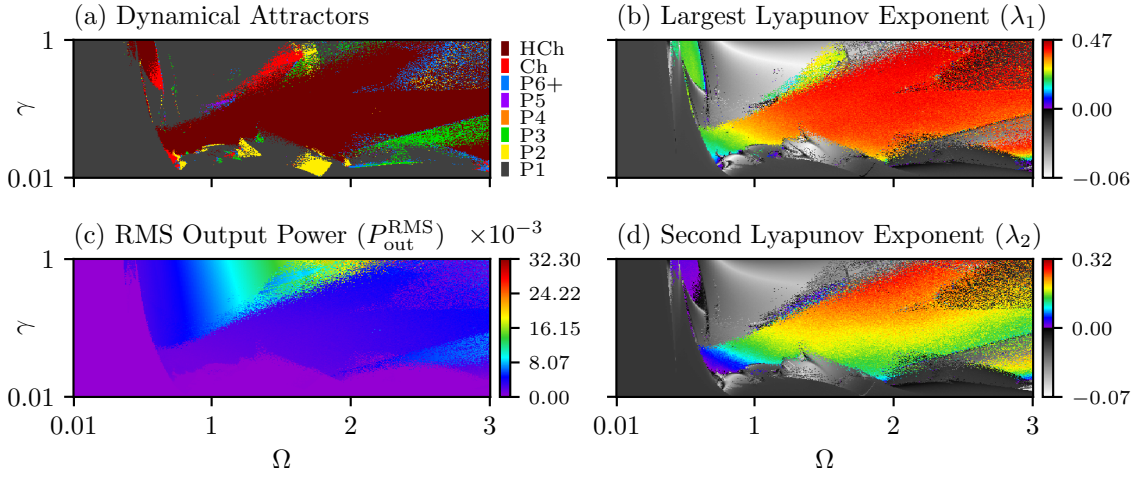

Figure 4 – Equilibrium configuration D: (a) Attractors based on the dynamical response of the system. P# $(\#=1,2,3,4,5,6+)$ stands for periodic motion, while Ch and HCh shows chaotic and hyperchaotic motion, respectively; (b) Largest Lyapunov exponent (λ_1) diagram; RMS Output Power ($P_{\text{out}}^{\text{RMS}}$) diagram; (d) Second Lyapunov exponent (λ_2) diagram.

In terms of complexity, the configuration D can be more difficult to be set up than the basic configuration, since the number of system equilibrium points triplicate, meaning that the number of system responses can be vast. It should be noticed that the system dynamics starts in a stable equilibrium point (at rest), and each one of the 501x501 samples represented in the diagrams can present at least 4 different solutions; even if those solutions present the same dynamical response, they are still different compared to each other. In this paper, only solutions related to one initial condition based on a stable equilibrium point are evaluated. By considering the configuration D, it is used an EP_6 based initial value whereas for the basic configuration harvester an initial value based on EP_2 was utilized. In this regard, some $\bar{z}_1$-$\dot{\bar{z}}_1$, $\bar{z}_2$-$\dot{\bar{z}}_2$ and $\bar{z}_1$-$\bar{z}_2$ phase subspaces of the configuration D are illustrated in Figures 5 to 12, showing some of the dynamical attractors classified in the diagram. The classification colors are also followed in those examples and the respective points in the γ,Ω domain are highlighted.

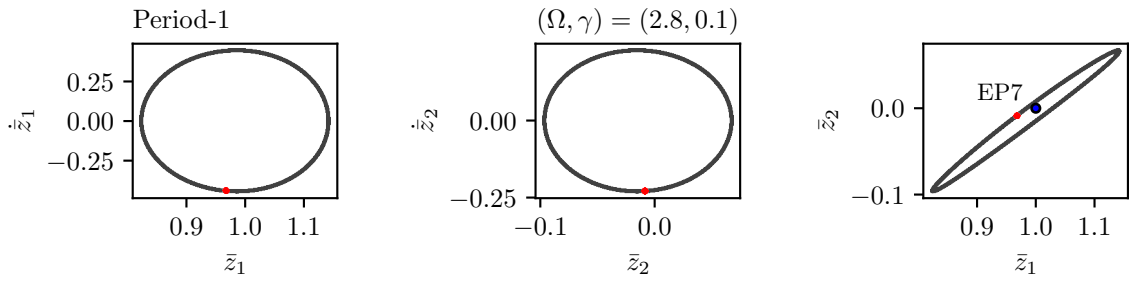

Figure 5 – Phase subspaces and Poincaré maps of a period-1 motion oscillating around EP_7.

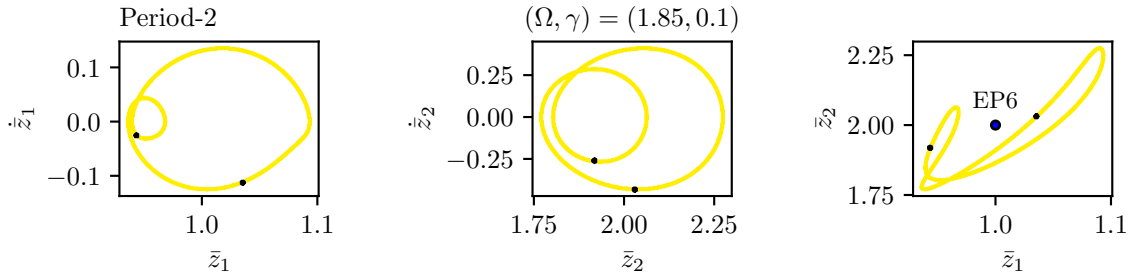

Figure 6 – Phase subspaces and Poincaré maps of a period-2 motion oscillating near EP_6.

Figure 5 shows a steady state period-1 response with $(\Omega, \gamma) = (2.8, 0.1)$, which is an example of a dynamical behavior that starts at EP_6 and finishes at EP_7. In contrast, Figure 6 represents a scenario in which the system starts at EP_6 and finishes oscillating near its initial condition with period-2 motion. These equilibrium point changes occur due to the transient dynamics, showing different possibilities even for similar patterns of motion.

A period-3 motion is shown in Figure 7, exemplifying a scenario in which the system starts at EP_6 and finishes oscillating around EP_8. Additionally, a complex pattern of period-4 motion is represented in Figure 8 also showing a steady-state motion based on EP_8, but instead of oscillating around the equilibrium position, it moves near and through EP_8.

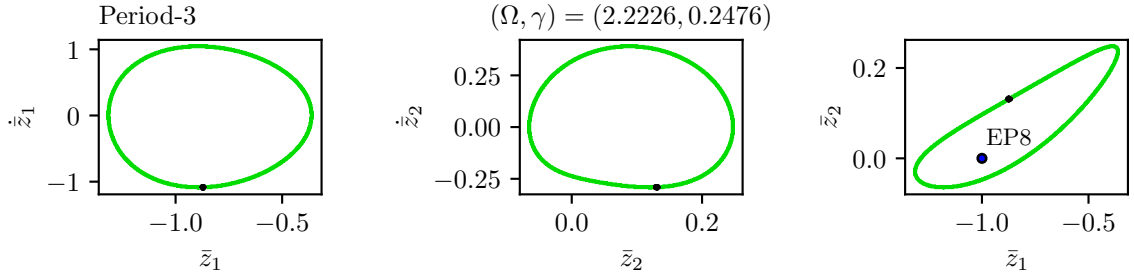

Figure 7 – Phase subspaces and Poincaré maps of a period-3 motion oscillating around EP_8.

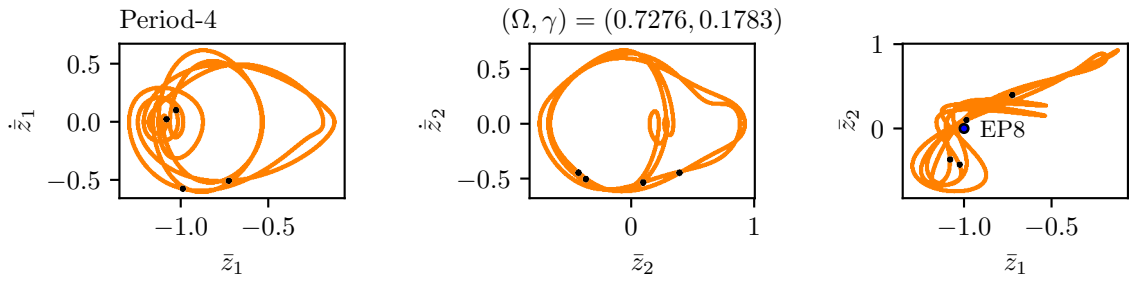

Figure 8 – Phase subspaces and Poincaré maps of a period-4 motion oscillating through EP_8.

Until now, it has been shown that patterns are associated with dynamics that goes from one stable equilibrium position to another one. Nevertheless, it is not always the case. Figure 9 shows a scenario of period-5 response presenting a larger amplitude of motion that oscillates around and through many equilibrium positions.

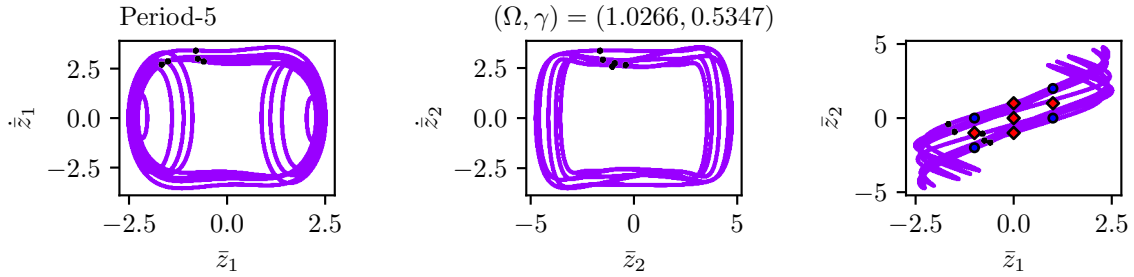

Figure 9 – Phase subspaces and Poincaré maps of a period-5 motion oscillating around and through many EPs.

Although the developed analysis is an interesting framework for a parametric analysis, it depends on the range of values of the parameter domain and on the number of forcing periods (range of time) analyzed. In some cases, the identified responses are still in transient motion, which may induce some misunderstandings about the type of steady state motion. This is the case shown in Figure 10, in which the attractor seems to converge to a period-1 orbit when it reaches the steady state regime. It is also interesting to observe that, due to the scarcity of period-4 and period-5 large areas, and the non-robustness of certain areas of period-3 and period-6+ in the dynamical response diagram, it is necessary to specify more precisely (Ω, γ) to find such behaviors.

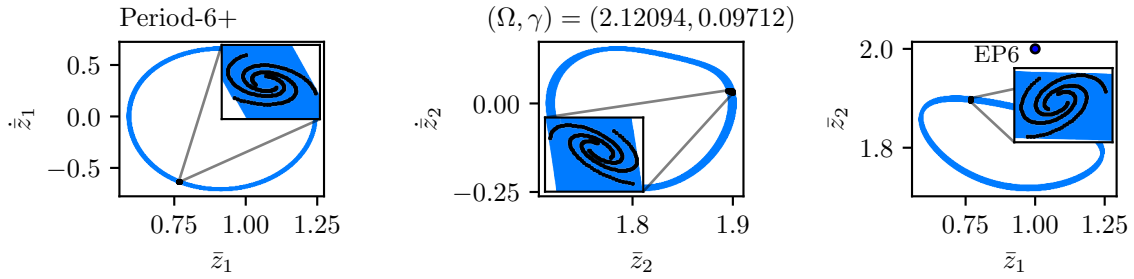

Figure 10 – Phase subspaces and Poincaré maps of an apparent period-6+ motion oscillating near EP_6.

Figure 11 shows a chaotic attractor while Figure 12 presents a hyperchaotic attractor. On both cases, an extended number of forcing periods ($n_p = 100000$) are analyzed to highlight the fractal-like characteristic of the chaotic attractor and the blurred characteristic of the hyperchaotic attractor. It is also interesting to notice that the chaotic dynamics occurs around one stable equilibrium point.

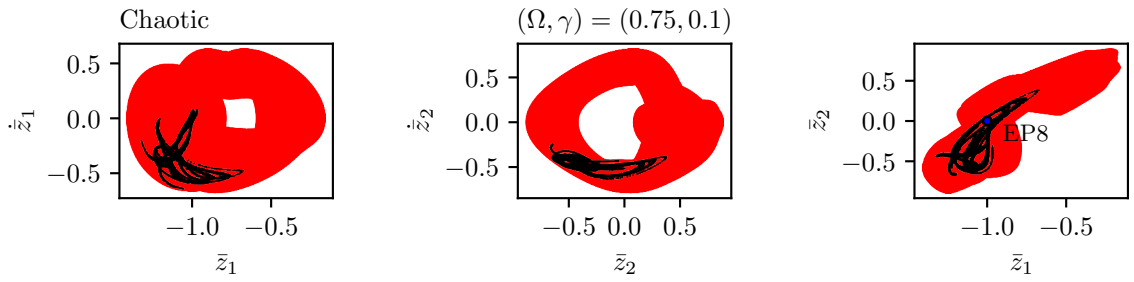

Figure 11 – Phase subspaces and Poincaré maps of a chaotic motion oscillating around EP_8.

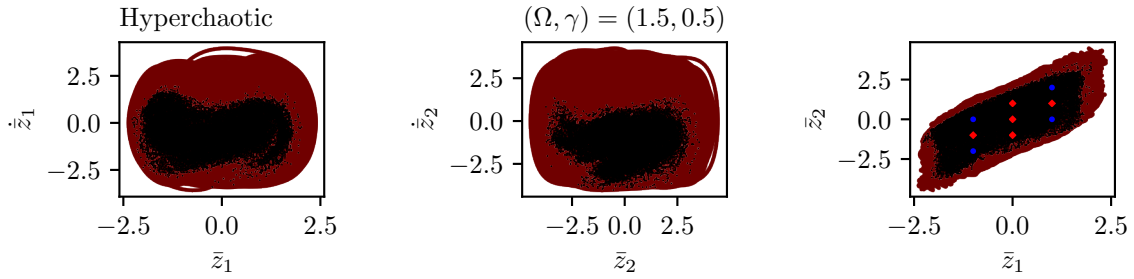

Figure 12 – Phase subspaces and Poincaré maps of a Hyperchaotic motion oscillating around all equilibrium positions.

A performance analysis of the energy harvested by the system is now in focus. Comparing the RMS Output Power $P_{\text{out}}^{\text{RMS}}$ of the two devices (Figures 3(c) and 4(c)), it is evident the difference between both systems. In terms of maximum output power, the basic configuration device is ≈ 10 times better in a specific short range of frequencies. However, in terms of bandwidth, the configuration D is more advantageous, even if it shows a smaller maximum output power. Still, as the power output magnitudes presented for the two configurations are too discrepant to compare, it is important to analyze each 501x501 cases of each configuration separately. For that, consider the error metric defined by:

$$\%\,\text{Error} = \frac{P_{\text{out}}^{\text{RMS}}(D) - P_{\text{out}}^{\text{RMS}}(Basic)}{P_{\text{out}}^{\text{RMS}}(Basic)} \times 100 \tag{33}$$

which compares the power output of the configuration D harvester with the power output of the basic configuration. Figure 13 summarizes the results: rainbow colors represents in percentage cases when the configuration D outperforms the basic configuration harvester, while grayscale colors represent situations in which the opposite is true. Thus, it shows that the proposed configuration D in this paper outperforms the basic configuration device in almost all results in higher frequencies, specially in the lower values of $0.1 < \gamma < 0.5$, region that the proposed configuration D device achieves better performances of 2000% or greater.

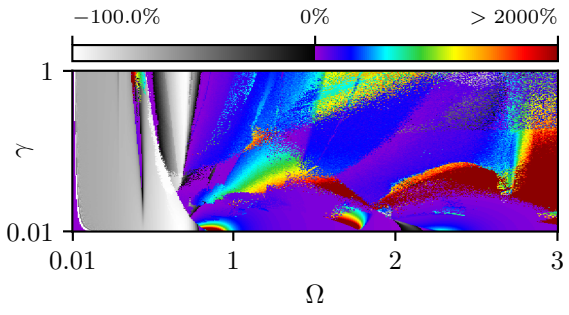

Figure 13 – Performance comparison between the RMS Output Power ($P_{\text{out}}^{\text{RMS}}$) of the configuration D and the basic configuration energy harvesters.

CONCLUSIONS

This work presents the analysis a Duffing-type two-degree of freedom energy harvesting system. A theoretical model is developed and ideal cases in which the properties of each degree of freedom are equal is analyzed. Stability analysis shows that the system is composed by 9 equilibrium points, being 4 stable and 5 unstable. Classic nonlinear dynamics tools as Poincaré maps and Lyapunov exponents are employed to determine the different types of dynamical responses of the system. Diagrams are then built to summarize the system dynamics in a parametric domain composed by a range of values of external forcing frequency and amplitude. Results show a complex dynamics with the predominance of robust zones of period-1, period-2, chaotic and hyperchaotic responses, and a non-robust zone of period-3 responses. Also, the occurrence of dynamical changes among equilibrium points are shown in a variety of cases. In terms of performance, the RMS output power measure is used as basis. Analyses show that the proposed system presents an interesting bandwidth, being an good option to be utilized to harvest energy at higher frequencies, especially for lower-mid values of forcing amplitude.

ACKNOWLEDGMENTS

The authors would like to acknowledge the support of the Brazilian Research Agencies CNPq, CAPES and FAPERJ.

REFERENCES

Costa, L.G., da Silva Monteiro, L.L., Pacheco, P.M.C.L. and Savi, M.A., 2021. “A parametric analysis of the nonlinear dynamics of bistable vibration-based piezoelectric energy harvesters”. Journal of Intelligent Material Systems and Structures, Vol. 32, No. 7, pp. 699–723.

Curie, P., 1889, “Dilatation Électrique du Quartz”. Journal de Physique Théorique et Appliquée, Vol. 8, No. 1, pp. 149–168.

Erturk, A. and Inman, D. J., 2008, ”On Mechanical Modeling of Cantilevered Piezoelectric Vibration Energy Harvesters, Journal of Intelligent Material Systems and Structures”, Vol. 19, pp. 1311-1325.

Kumar, K.A., Ali, S.F. and Arockiarajan, A., 2015. “Piezomagnetoelastic broadband energy harvester: Nonlinear modeling and characterization”, The European Physical Journal Special Topics, Vol. 224, No. 14, pp. 2803–2822.

Margielewicz, J., Gaska, D., Litak, G., Wolszczak, P. and Yurchenko, D., 2022, “Nonlinear dynamics of a new en- ergy harvesting system with quasi-zero stiffness”, Applied Energy, Vol. 307, p. 118159.

Meirovitch, L., 2010, ”Methods of Analytical Dynamics”. Advanced engineering series. Dover Publications.

Preumont, A., 2006, ”Mechatronics: Dynamics of Electromechanical and Piezoelectric Systems”, Springer Netherlands, Dordrecht.

Savi, M., 2017, ”Dinâmica Não-linear E Caos”, E-papers.

Tang, L. and Yang, Y., 2012, ”A multiple-degree-of-freedom piezoelectric energy harvesting model”, Journal of Intelligent Material Systems and Structures, Vol. 23, No. 14, pp. 1631–1647.

Wolf, A., Swift, J.B., Swinney, H.L. and Vastano, J.A., 1985, “Determining Lyapunov exponents from a time series”, Physica D, Vol. 16, No. 3, pp. 285–317.

Wu, H., Tang, L., Yang, Y. and Soh, C. K., 2012, ”A novel two-degrees-of-freedom piezoelectric energy harvester”, Journal of Intelligent Material Systems and Structures Vol. 24, No. 3, pp. 357–368

Wu, H., Tang, L., Yang, Y. and Soh, C. K., 2014, ”Development of a broadband nonlinear two-degree-of-freedom piezoelectric energy harvester”, Journal of Intelligent Material Systems and Structures, Vol. 25, No. 14, pp. 1–15.

RESPONSIBILITY NOTICE

The authors are the only parties responsible for the printed material included in this paper.